nanomaterials

MDPI

Article

Blasius–Rayleigh–Stokes Flow of Hybrid Nanomaterial Liquid Past a Stretching Surface with Generalized Fourier's and Fick's Law

Yingzi Jiang [1], Juan Zhang [2], Thabet Abdeljawad [3,4,*], Shafiq Ahmad [5,*], Muhammad Naveed Khan [5], Aysha Rehman [6], Abdulrazak H. Almaliki [7] and Ahmed S. El-Shafay [8,9]

1 School of Mathematics and Statistics, Xuzhou Institute of Technology, Xuzhou 221018, China; xzitjyz@163.com
2 Guangdong ATV Vocational College for the Performing Arts, Dongguan 523710, China; zj801106@163.com
3 Department of Mathematics and Sciences, Prince Sultan University, Riyadh 11586, Saudi Arabia
4 Department of Medical Research, China Medical University, Taichung 40402, Taiwan
5 Department of Mathematics, Quaid-I-Azam University, Islamabad 44000, Pakistan; mnkhan@math.qau.edu.pk
6 Department of Mathematics, University of Gujrat, Gujrat 50700, Pakistan; aysharehman1986@gmail.com
7 Department of Civil Engineering, College of Engineering, Taif University, P.O. Box 11099, Taif 21944, Saudi Arabia; a.almaliki@tu.edu.sa
8 Department of Mechanical Engineering, College of Engineering, Prince Sattam Bin Abdulaziz University, Alkharj 16273, Saudi Arabia; a.abdou@psau.edu.sa
9 Mechanical Power Engineering Department, Faculty of Engineering, Mansoura University, Mansoura 35516, Egypt
* Correspondence: tabdeljawad@psu.edu.sa (T.A.); ashafiq@math.qau.edu.pk (S.A.)

Abstract: The effect of Stefan blowing on the Cattaneo–Christov characteristics of the Blasius–Rayleigh–Stokes flow of self-motive Ag-MgO/water hybrid nanofluids, with convective boundary conditions and a microorganism density, are examined in this study. Further, the impact of the transitive magnetic field, ablation/accretion, melting heat, and viscous dissipation effects are also discussed. By performing appropriate transformations, the mathematical models are turned into a couple of self-similarity equations. The bvp4c approach is used to solve the modified similarity equations numerically. The fluid flow, microorganism density, energy, and mass transfer features are investigated for dissimilar values of different variables including magnetic parameter, volume fraction parameter, Stefan blowing parameter, thermal and concentration Biot number, Eckert number, thermal and concentration relaxation parameter, bio-convection Lewis parameter, and Peclet number, to obtain a better understanding of the problem. The liquid velocity is improved for higher values of the volume fraction parameter and magnetic characteristic, due to the retardation effect. Further, a higher value of the Stefan blowing parameter improves the liquid momentum and velocity boundary layer thickness.

Keywords: Blasius–Rayleigh–Stokes flow; hybrid nanofluid; generalized Fourier's and Fick's law; transitive magnetic field

check for updates

Citation: Jiang, Y.; Zhang, J.; Abdeljawad, T.; Ahmad, S.; Naveed Khan, M.; Rehman, A.; Almaliki, A.H.; El-Shafay, A.S. Blasius–Rayleigh–Stokes Flow of Hybrid Nanomaterial Liquid Past a Stretching Surface with Generalized Fourier's and Fick's Law. *Nanomaterials* **2022**, *12*, 439. https://doi.org/10.3390/nano12030439

Academic Editors: Manuel M. Piñeiro and Lou Kondic

Received: 15 November 2021
Accepted: 25 January 2022
Published: 27 January 2022

Publisher's Note: MDPI stays neutral with regard to jurisdictional claims in published maps and institutional affiliations.

1. Introduction

At present, researchers are keen to study heat transfer applications involving nanofluids. Based on empirical results in various technical and medical fields, the heat transport, mass, and density during the flow have dynamic features. Many base liquids are not favorable for heat transfer applications due to poor thermal effectiveness. To overcome this problem and improve the heat transfer efficiency, we added nanoparticles to the base fluids. The nano-size particles are most effective in enhancing the heat transfer rate. These nanoparticles consist mostly of metals such as silver, steel, gold, copper, potassium, nitrides, and many others. Choi [1] was the first to introduce the theory of nanofluids. Later,

Buongiorno [2] discussed the concept of natural convective heat transport in a nanofluid. Sheikholeslami and Chamkha [3] explored the Lorentz force effect on the nanofluid flow. Ahmad et al. [4] introduced the influence of carbon nanotube nanoparticles on the boundary layer flow with thermal radiation, double stratification, and heat generation. They found that the thermal stratification diminished the temperature distribution. The natural convection heat transfer and inclined magnetic field effects of a molybdenum disulfide (MoS2) and magnesium oxide (MgO) nanofluid were investigated by Hymavathi et al. [5] via a vertical stretched surface embedded in a porous medium with a non-uniform heat source or sink. Nadeem et al. [6] used a magnetic dipole with three different ferrite nanoparticles to assess the effects of heat transport phenomena in a ferrofluid. They discovered that the characteristic of magneto-thermomechanical cooperation reduced the movement of liquid molecules, and as a result, increased the coefficient of skin friction and the thermal transport rate at the surface. Together with the impacts of viscous dissipation and non-linear thermal radiative effects, Reddy et al. [7] investigated the role of gyrotactic microorganisms in the mass and heat transport for the time-dependent MHD flow of a cross liquid mediated through nanoparticles. Vajravelu et al. [8] evaluated the influence of the nanoparticle volume fraction on the flow and heat transfer characteristics of Ag–water and Cu–water nanofluids under the impact of internal heat absorption or generation and thermal buoyancy. Jamshed et al. [9] explored the Casson non-Newtonian Cu–water and TiO_2–water nanofluid flows in terms of heat transport and entropy generation under the influence of solar thermal transfer and slip conditions. Many researchers (see [10–12]) have recently observed an improvement in the heat transport rate in the presence of various nanoparticles.

Many investigators have studied nanofluids to date, but studies related to hybrid nanofluids are attracting the attention of numerous scientists due to a wider range of heat conductivity applications. The combination of two or more nanoparticles in the base liquid generates a hybrid nanomaterial liquid. The reason that researchers are giving attention to this issue is the heat transport augmentation that can be accomplished by these hybrid nanofluids at a low cost of production. Mingzheng et al. [13] demonstrated the viscosity and thermal conductivity of various kinds of surfactant mixtures. Ahmad et al. [14] explored the thermal transport characteristics of a hybrid nanomaterial liquid with activation energy on a wedge, with the availability of variable velocity, Darcy–Forchheimer flow, and thermal slip. The influence of suction and buoyancy force effects on a Ag–MgO/water hybrid nanofluid flow across a stretching surface was introduced by Anuar et al. [15]. Maskeen et al. [16] explored the thermal transport properties of magneto-hydrodynamic hybrid alumina–copper/water nanomaterial liquid flow on an extending cylinder, with the influence of radiation and Joule heating. Ghalambaz et al. [17] demonstrated the thermal transport enhancement in a hybrid (Ag + MgO) nanofluid past a porous square cavity, using the local thermal non-equilibrium (LTNE) model. Manna et al. [18] proposed a new multi-banded magnetic field approach for improving the controllability of convective transports. Applying four equal parts of a magnetic field horizontally over a heated system occupied by porous material saturated with Cu–Al_2O_3/water hybrid nano liquid demonstrates the multi-banding approach. Ahmad and Nadeem [19] examined the properties of mass and heat transport in the presence of hybrid SWCNT–MWCNT/water nanomaterial liquid with Hall slip, ion slip, and chemical reaction impacts. Esfe et al. [20] scrutinized the impact of the volume fraction of nanoparticles on the dynamic viscosity and thermal conductivity of Ag–MgO/water hybrid nanofluids with particle sizes of 25(Ag) and 40(MgO) nm and nanofluid volume fractions (50 percent Ag and 50 percent MgO by volume) ranging from 0 to 2 percent and found new interrelations. In a modified Buongiorno's model for the nanomaterial liquid magneto-transport phenomenon over an expanding cylinder in the vicinity of motile microorganism density, Rana et al. [21] integrated the Cattaneo–Christov mass flux (non-Fick's) and heat (non-Fourier's) ideas. Ma et al. [22] provided a (2D) numerical simulation of Ag–MgO nanomaterial forced convection and thermal transport in

a channel with active coolers and heaters, to investigate the effect of a magnetic field on heat transport and nanomaterial liquid Ag–MgO forced convection.

Mass and heat transport phenomena occur due to the temperature and mass gradient respectively. Heat and mass transport have many industrial and engineering applications such as in heat exchangers, nuclear plants, heat pumps, heat conduction in tissues, refrigeration, heat transfer through materials, the diffusion of chemical impurities in rivers and oceans, the evaporation of water, etc. The convectional laws for the analysis of mass and heat transport used were Fourier's [23] and Fick's [24] laws. Fourier's and Fick's laws have a disadvantage; they give a parabolic type of energy and mass equation. To overcome this drawback, Cattaneo [25] modified Fick's and Fourier's laws by the addition of a time factor. Later, Christov [26] altered the Cattaneo law by replacing the time factor with the Oldroyd-B upper convective derivative. Han et al. [27] investigated the Maxwell liquid flow on a stretchable surface to present an evaluation of the Fourier heat flux and the Cattaneo–Christov model. With the addition of chemical reactions, a uniform heat source/sink, and thermal radiation, Venkateswarlu et al. [28] explored the impacts of a magnetic field on the flow of the Cattaneo–Christov heat flux model for MoS2 and MgO water-based nanofluids across a stretching sheet. Ali et al. [29] introduced the impact of the Cattaneo–Christov characteristics and bioconvection on self-motivated microorganisms in water-based nanoparticles with a leading-edge accretion/ablation and the Stefan blowing effect. The heat transport with respect to the Cattaneo–Christov concept with variable thermal relaxation time past a stretching sheet was discussed by Ahmad et al. [30]. Raju et al. [31] illustrated the heat, flow, and transport of mass attributes of a Maxwell nanofluid through a cylinder with a heat sink/source, using the Cattaneo–Christov premise. The Cattaneo–Christov premise was utilized by Malik et al. [32] to investigate the performance of Sisko fluid via a porous non-linearly stretched cylinder. Using a simplified mathematical model published by Jamshed and Aziz [33], the entropy production and heat transfer analysis of a thermal system containing hybrid nanomaterial with a Cattaneo–Christov flow model and thermal radiation impacts was explored. Garia et al. [34] used an extending surface with Joule heating and thermal radiation to solve the magneto-hydrodynamic flow of a SiO_2-MoS_2/water hybrid nanofluid past a wedge and a cone, with a generalized Fourier's model.

The transport of electric current through any conducting material produces Joule heating. The collision of moving particles is the reason behind this. As a result of this process, some kinetic energy is transformed to heat, and the temperature of the material rises. Scientists and engineers have been fascinated by the idea of improving the efficiency of numerous mechanical systems and industrial machinery in recent years. Such problems can be overcome by lowering the temperature induced by Ohmic dissipation or Joule heating. As a result, several academics studied the flow issues from diverse physical perspectives. Sahoo [35] explored the impacts of partial slip and Joule heating on the flow of second-grade MHD liquid on a stretched surface with thermal transmission. Shehzad et al. [36] reported the radiative MHD extended flow of a Jeffrey liquid with Joule heating. Waqas et al. [37] discussed the Carreau–Yasuda nanomaterial liquid flow past an extending/shrinking surface in the presence of Joule heating, motile microorganisms, and thermal radiation, under Robin's conditions. In the presence of thermal radiation and Joule heating, Kumar et al. [38] evaluated the 3D Oldroyd-B nanofluid flow across a stretching sheet. Hayat et al. [39] investigated the 3D steady second-grade nanomaterial flow via a rotating disc, with Joule heating and heat generation/absorption. For the constant wall heat flux condition, Chakraborty et al. [40] critically evaluated the transport-of-heat performance related to thermally developed coupled-electron magneto-hydrodynamic flows towards narrow flow conduits, taking electrokinetic impacts into account. Chen [41] conducted a study to investigate the impacts of Joule heating and viscous dissipation on the thermal transport and momentum, for magneto-hydrodynamic (MHD) flow towards an extending surface in the presence of radiation and surface suction/blowing.

Technical engineers, designers, manufacturers, and developers are keen to study Blasius–Rayleigh–Stokes flow. To transform the time-dependent flow model's partial differential equations into a similar form, a new type of transformation was developed by Na [42], which consists of the Blasius–Rayleigh–Stokes variables. Fang [43] analyzed the heat transportation in an unsteady flow with the implementation of Blasius–Rayleigh–Stokes variables on a flat surface. Todd [44] was the first to establish the concept of leading-edge accretion/ablation, which is based on the unstable boundary layer model. The influence of radiation, Joule heating, and the Cattaneo–Christov theory applied to a Blasius–Rayleigh–Stokes flow towards a transitive magnetic field was discussed by Reddy et al. [45]. Several scholars have published studies on the Blasius–Rayleigh–Stokes variables in recent decades [46,47].

The unsteady MHD stagnation point Blasius-Rayleigh-Stokes hybrid nanomaterial liquid flow with Cattaneo-Christov theory, Joule heating, and convective conditions effect over an extending surface were investigated. To the best of our knowledge, no study has yet investigated the Blasius–Rayleigh–Stokes flow of hybrid nanomaterial liquid with convective boundaries. The Blasius–Rayleigh–Stokes variables were applied to transport the flow model into a couple of ODEs. The bvp4c MATLAB approach [48,49] was applied to solve these multiple equations numerically. The evolving parameters are discussed graphically along with the velocity, microorganism density, temperature, and concentration distribution. Further, a tabulated analysis of physical quantities is presented. To validate the problem, a comparison table is presented.

2. Mathematical Modeling

We consider the unsteady, laminar, incompressible, viscous, 2D, MHD boundary layer of the stagnation point Blasius–Rayleigh–Stokes flow of a hybrid nanofluid in the presence of viscous dissipation and microorganism density. The thermal and solutal energy transport analyses are presented with the influence of the Cattaneo–Christov theory and Joule heating. Furthermore, convective boundary conditions are applied on the surface of the stretching sheet and free-stream conditions are considered away from the surface. The transitive magnetic field is applied normally to the flow field. The free-stream and fluid velocities are U_∞ and U_w, respectively, as shown in Figure 1. The fluid microorganism density, concentration, and temperature are N, C, and T, respectively. The wall temperature is T_w, the wall concentration is C_w, and the wall microorganism density is N_w; away from the wall these terms are T_∞, C_∞, and N_∞, respectively. Using the boundary layer approximation of $O_{(u)} = 1 = O_{(x)}$, $O_{(v)} = \delta = O_{(y)}$ and the above supposition, the equations of momentum, mass, energy, concentration, and microorganism density become [11,21,45]:

$$\frac{\partial v}{\partial y} + \frac{\partial u}{\partial x} = 0, \tag{1}$$

$$\frac{\partial u}{\partial t} + v\frac{\partial u}{\partial y} + u\frac{\partial u}{\partial x} - U_\infty \frac{\partial U_\infty}{\partial x} - \frac{\partial U_\infty}{\partial t} = \nu_{hnf}\frac{\partial^2 u}{\partial y^2} + \frac{\sigma_{hnf}B^2}{\rho_{hnf}}\sin^2\alpha u, \tag{2}$$

$$\begin{gathered}\frac{\partial T}{\partial t} + \frac{\partial T}{\partial x}u + \frac{\partial T}{\partial y}v = \alpha^*_{hnf}\frac{\partial^2 T}{\partial y^2} + \frac{\sigma_{hnf}B^2}{(\rho C_p)_{hnf}}\sin^2\alpha u^2 + \frac{\mu_{hnf}}{(\rho C_p)_{hnf}}\left(\frac{\partial u}{\partial y}\right)^2 \\ -\lambda_1\left(\frac{\partial^2 T}{\partial t^2} + \frac{\partial u}{\partial t}\frac{\partial T}{\partial x} + \frac{\partial v}{\partial t}\frac{\partial T}{\partial y} + u^2\frac{\partial^2 T}{\partial x^2} + \left(u\frac{\partial v}{\partial x} + v\frac{\partial v}{\partial y}\right)\frac{\partial T}{\partial y} + v^2\frac{\partial^2 T}{\partial y^2} + \left(v\frac{\partial u}{\partial y} + u\frac{\partial u}{\partial x}\right)\frac{\partial T}{\partial x}\right) \\ -2\lambda_1\left(u\frac{\partial^2 T}{\partial t\partial x} + v\frac{\partial^2 T}{\partial t\partial y} + uv\frac{\partial^2 T}{\partial x\partial y}\right),\end{gathered} \tag{3}$$

$$\begin{gathered}\frac{\partial C}{\partial t} + \frac{\partial C}{\partial x}u + \frac{\partial C}{\partial y}v + \lambda_2\left(\frac{\partial^2 C}{\partial t^2} + \frac{\partial u}{\partial t}\frac{\partial C}{\partial x} + \frac{\partial v}{\partial t}\frac{\partial C}{\partial y} + u^2\frac{\partial^2 C}{\partial x^2} + v^2\frac{\partial^2 C}{\partial y^2}\right) = D_m\frac{\partial^2 C}{\partial y^2} \\ -2\lambda_2\left(u\frac{\partial^2 C}{\partial t\partial x} + v\frac{\partial^2 C}{\partial t\partial y} + uv\frac{\partial^2 C}{\partial x\partial y}\right) - \lambda_2\left(u\frac{\partial v}{\partial x} + v\frac{\partial v}{\partial y}\right)\frac{\partial C}{\partial y} - \lambda_2\left(v\frac{\partial u}{\partial y} + u\frac{\partial u}{\partial x}\right)\frac{\partial C}{\partial x},\end{gathered} \tag{4}$$

$$\frac{\partial N}{\partial t} + \frac{\partial N}{\partial x}u + \frac{\partial N}{\partial y}v = -\frac{bW_c}{C_w - C_\infty}\frac{\partial}{\partial y}\left(N\frac{\partial C}{\partial y}\right) + D_n\frac{\partial^2 N}{\partial y^2}, \tag{5}$$

and the related boundary conditions are [29]:

$$\left.\begin{array}{l} u = 0, -k_{hnf}\frac{\partial T}{\partial y} = h_f(T_w - T), -D_m\frac{\partial C}{\partial y} = h_g(C_w - C), \\ -D_n\frac{\partial N}{\partial y} = h_n(N_w - N), v = v_w = \frac{D_m}{1-C_w}\left(\frac{\partial C}{\partial y}\right), \text{ as } y = 0, \end{array}\right\} \quad (6)$$

$$u \to U_\infty, T \to T_\infty, N \to N_\infty, C \to C_\infty, \text{ as } y \to \infty. \quad (7)$$

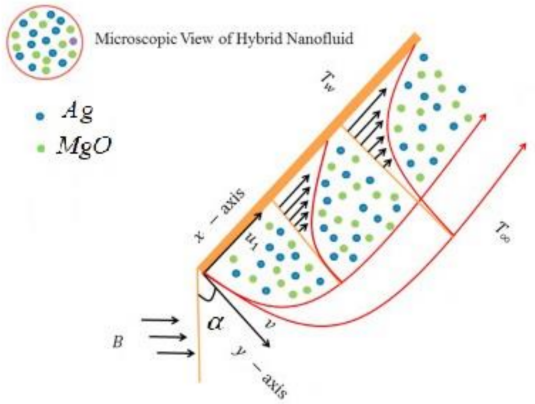

Figure 1. Problem configuration.

In the above equations, σ_{inf} is the electrical conductivity of the nanofluid, the density of the nanomaterials liquid is ρ_{inf}, the kinematic viscosity of the nanomaterials liquid is v_{inf}, the magnetic field is B, the thermal diffusion coefficient is α^*_{inf}, the microorganism concentration and diffusivity coefficient are D_m and D_n, respectively, h_f, h_g, and h_n are the heat, mass, and microorganism transport coefficient, respectively, λ_1 and λ_2 are the thermal and concentration time relaxations, respectively, W_c signifies the cell swimming speed, and b symbolizes the chemotaxis constant.

2.1. Similarity Analysis

Using the similarity transformation [29,44,45]:

$$\zeta = y/\sqrt{\cos(w^*)v_f t + \sin(w^*)\left(\frac{v_f x}{U_\infty}\right)},\ \theta(\zeta) = \frac{T - T_\infty}{T_w - T_\infty}, g(\zeta) = \frac{C - C_\infty}{C_w - C_\infty}, \quad (8)$$

$$h(\zeta) = \frac{N}{N_w}, u = u_w f'(\eta), v = \frac{(v_f/2)(\zeta f'(\zeta) - f(\zeta))\sin(w^*)}{\sqrt{\cos(w^*)v_f t + \sin(w^*)\left(\frac{v_f x}{U_\infty}\right)}}, \quad (9)$$

Applying Equation (7), the above nanoparticle phase equation transmutes to:

$$\frac{\mu_r}{\rho_r}f''' + \frac{1}{2}\cos(w^*)\zeta f'' + \frac{1}{2}\sin(w^*)ff'' + \frac{M\sigma_r}{\rho_r}\sin^2\alpha(1 - f') = 0, \quad (10)$$

$$\begin{aligned}\frac{k_r}{(\rho C)_r}\theta'' + \frac{\Pr}{2}\left(\zeta\theta'\cos(w^*) + f\sin(w^*)\theta' + \gamma_e\sin(w^*)\left(3ff'\theta' + \zeta f\theta''\right)\right) \\ + \frac{E_c M\sigma_r}{(\rho C)_r}\sin^2\alpha f'^2 + \frac{E_c\mu_r}{(\rho C)_r}f''^2 = 0,\end{aligned} \quad (11)$$

$$g'' + \frac{\Pr L_e}{2}\left(\zeta\cos(w^*)g' + f\sin(w^*)g' + \gamma_c\sin(w^*)\left(3ff'g' + \zeta fg''\right)\right) = 0, \quad (12)$$

$$h'' + \frac{\Pr L_b}{2}\left(\zeta\cos(w^*)h' + f\sin(w^*)h'\right) - P_e\left(hg'' + h'g'\right) = 0, \quad (13)$$

The transformed conditions are:

$$\left.\begin{array}{c} f'(0)=0, f(0)=\frac{2s}{L_e \mathrm{Pr}\sin w^*}g,\ k_r\theta'(0)=-B_e(1-\theta(0)), \\ g'(0)=-B_c(1-g(0)), h'(0)=-B_n(1-h(0)), \end{array}\right\} \tag{14}$$

$$f'(\zeta)\to 1, \theta(\zeta)\to 0,\ g(\zeta)\to 0, h(\zeta)\to 0,\ \text{at}\ \zeta\to\infty, \tag{15}$$

The parameters ablation/accretion, thermal Biot number, Lewis number, concentration Biot number, microorganism Biot number, magnetic field parameter, bio-convection Lewis number, Stefan blowing parameter, Eckert number, thermal relaxation parameter, concentration relaxation parameter, Peclet number, and solid volume fraction of particles are symbolized by w^*, B_e, L_e, B_c, B_n, M, L_b, s, E_c, γ_e, γ_c, P_w and ϕ_1, respectively. These parameters are defined as:

$$\gamma_e=\lambda_1 U_\infty, \gamma_c=U_\infty\lambda_2, \mathrm{Pr}=\frac{v_f}{\alpha_f}, L_e=\frac{v_f}{D_m}, M=\frac{\sigma_f {B_0}^2}{\rho_f}, \tag{16}$$

$$L_b=\frac{v_f}{D_n}, E_c=\frac{{u_w}^2}{C_p(T_w-T_\infty)},\ s=\frac{(C_w-C_\infty)}{(1-C_w)}, B_t=-\frac{h_f}{k_f}\sqrt{\frac{v_f}{\alpha_f}}, \tag{17}$$

The hypothetical relation is characterized as follows [20–22].

$$\sigma_r=\frac{\sigma_{hnf}}{\sigma_f}=\left[\frac{1+3\left(\frac{\sigma}{\sigma_f}-1\right)\left(\phi_{MgO}+\phi_{Ag}\right)}{\left(\frac{\sigma}{\sigma_f}+2\right)-\left(\frac{\sigma}{\sigma_f}-1\right)\left(\phi_{MgO}+\phi_{Ag}\right)}\right], \tag{18}$$

$$(\rho c)_r=\frac{(\rho c)_{hnf}}{(\rho c)_f}=\left(1+\phi_{MgO}-\phi_{Ag}\right)+\phi_{Ag}\frac{(\rho c)_{Ag}}{(\rho c)_f}+\phi_{MgO}\frac{(\rho c)_{MgO}}{(\rho c)_f}, \tag{19}$$

$$\rho_r=\frac{\rho_{hnf}}{\rho_f}=\left(1+\phi_{MgO}-\phi_{Ag}\right)+\phi_{Ag}\frac{\rho_{Ag}}{\rho_f}+\phi_{MgO}\frac{\rho_{MgO}}{\rho_f}, \tag{20}$$

$$\mu_r=\frac{\mu_{hnf}}{\mu_f}=\left[1+32.795\phi_1-7214\phi_1^2+714600\phi_1^3-0.1941\times 10^8\phi_1^4\right]; \quad 0\le\phi_1\le 0.02, \tag{21}$$

$$k_r=\frac{k_{hnf}}{k_f}=\left[\frac{0.1747\times 10^5+\phi_1}{0.1747\times 10^5-0.1498\times 10^6\phi_1+0.1117\times 10^7\phi_1^2+0.1997\times 10^7\phi_1^3}\right]; \quad 0\le\phi_1\le 0.03. \tag{22}$$

2.2. Quantities of Interest

The local friction drag and the local density number of motile microorganisms are:

$$C_f=\frac{\mu_{hnf}}{\rho_f {u_\infty}^2}\left[\frac{\partial u}{\partial y}\right]_{y=0}, Nn_x=\frac{-x}{N_w}\left[\frac{\partial N}{\partial y}\right]_{y=0}, \tag{23}$$

Using Equation (10), the dimensionless form is,

$$\mathrm{Re}_x^{1/2}C_{fx}=\frac{\mu_r f''(0)}{\sqrt{\cos(w^*)\tau+\sin(w^*)}}, \mathrm{Re}_x^{-1/2}Nn_x=\frac{-h'(0)}{\sqrt{\cos(w^*)\tau+\sin(w^*)}}. \tag{24}$$

The local Reynolds number is characterized as $Re_x=\frac{xu_\infty}{v_f}$.

3. Numerical Method and Evidence

The MATLAB BVP4C functions are now used to obtain numerical solutions for nonlinear coupled ODEs (10)–(13) with boundaries (14) and (15). The MATLAB BVP4C functions can only solve first-order ODEs. We transformed the second- and third-order DEs to first-order DEs and chose a reasonable value of η_∞, where 10^{-6} was left aside as the absolute convergence threshold, and consequently the first-order classifications were:

$$f'' = y(3), f' = y(2), f = y(1),\ \theta' = y(5), \theta = y(4), g' = (7), g = y(6), h' = y(9), h = y(8), \tag{25}$$

$$yy1 = f''' = \frac{\rho_r}{\mu_r}\left\{-\frac{1}{2}\cos(w^*)\zeta y(3) - \frac{1}{2}\sin(w^*)y(1)y(3) - \frac{M\sigma_r}{\rho_r}\sin^2\alpha(1-y(2))\right\}, \tag{26}$$

$$yy2 = \theta'' = \frac{1}{\left\{\frac{k_r}{(\rho C)_r} + \frac{\Pr\gamma_e\zeta\sin(w^*)y(1)}{2}\right\}}\left\{\begin{array}{c} -\frac{\Pr}{2}(\zeta\cos(w^*)y(5) + \gamma_e\sin(w^*)(3y(1)y(2)y(5))) \\ -\frac{\Pr}{2}y(1)\sin(w^*)y(5) - \frac{E_cM\sigma_r}{(\rho C)_r}\sin^2\alpha y(2)^2 - \frac{E_c\mu_r}{(\rho C)_r}y(3)^2 \end{array}\right\}, \tag{27}$$

$$yy3 = g'' = \frac{1}{(1 + \frac{\Pr L_e\gamma_c\sin(w^*)\zeta y(1)}{2})}\left\{\begin{array}{c} -\frac{\Pr L_e}{2}(\zeta\cos(w^*)y(7) + y(1)\sin(w^*)y(7)) \\ -\frac{\Pr L_e}{2}\gamma_c\sin(w^*)(3y(1)y(2)y(7)) \end{array}\right\}, \tag{28}$$

$$yy4 = h'' = -\frac{\Pr L_b}{2}(\zeta\cos(w^*)y(9) + y(1)\sin(w^*)y(9)) + P_e(y(8)yy3 + y(9)y(7)), \tag{29}$$

with the conditions,

$$y_0(2); y_0(2) - \frac{2s}{L_e\Pr\sin w^*}y_0(6);\ k_r y_0(5) + B_e(1-y_0(4)); y_0(7) + B_c(1-y_0(6)); y_0(9) + B_n(1-y_0(8))\Big\}, \tag{30}$$

$$y_{\inf}(2) - 1;\ y_{\inf}(4);\ y_{\inf}(6); y_{\inf}(8); \tag{31}$$

In conclusion, $\eta_\infty = 6$ is used in this study to attain the asymptotic values provided by the boundary condition (14) and (15). Because the relationship determines a high level of comprehension for each considered value, we are confident that this conclusion is correct and precise. Table 1 shows that Nanoparticles (Ag, MgO) and base fluid (water) thermo-physical characteristics. Table 2 is a comparative analysis for given values of ω^* (ablation/accretion parameter) against the velocity gradient. It can be seen that larger values of ω^* improve the velocity gradient.

Table 1. Nanoparticles (Ag, MgO) and base fluid (water) thermo-physical characteristics [20–22].

Physical Properties	Base Fluid	Nanoparticle	
	Water	Ag	MgO
C_p (J/kgK)	4179.0	235	955
ρ (kg/m^3)	997.10	10,500	3560
k (W/mK)	0.620	429	45

Table 2. Comparative study of $f''(0)$ (velocity gradient) along with specific values of ω^* (ablation/accretion characteristic) when $s = 0$.

ω^*	Mabood et al. [47]	Todd et al. [44]	Ali et al. [29]	Our Results
0	0.564189	0.5642	0.564190	0.564191
$\pi/24$	0.575016	0.5750	0.575019	0.575020
$\pi/12$	0.580728	0.5807	0.580726	0.580727
$\pi/6$	0.577001	0.5770	0.577002	0.577003
$\pi/4$	0.552875	0.5529	0.552876	0.552877
$\pi/3$	0.507218	0.5072	0.507221	0.507222
$5\pi/12$	0.436864	0.4369	0.436867	0.436868
$11\pi/24$	0.389999	0.3900	0.390002	0.390003
$\pi/2$	0.332057	0.3321	0.332057	0.332058

4. Results and Discussion

In this section, the physical implications of prominent characteristics such as the magnetic characteristic $(0 \leq M \leq 3)$, Stefan blowing parameter $(0 \leq s \leq 6)$, solid volume fraction $(0 \leq \phi_1 \leq 0.03)$, thermal Biot number $(0 \leq B_e \leq 1.5)$, Eckert number $(I \leq E_c \leq 4)$, thermal relaxation parameter $(0 \leq \gamma_e \leq 0.3)$, concentration Biot number $(0.1 \leq B_c \leq 0.4)$, Lewis number $(1 \leq L_e \leq 5)$, concentration relaxation parameter $(0 \leq \gamma_c \leq 1.5)$, bio-convection Lewis parameter $(1 \leq L_b \leq 4$, Peclet number $(0 \leq P_e \leq 3)$, and microorganism Biot number $(1 \leq B_n \leq 3)$ against velocity, temperature, the volumetric concentration of nanoparticles, and motile microorganism number is reflected in Figures 3–16. Table 3 shows that higher values of ϕ_1 increase the skin friction, whereas higher estimates of M, α and s reduce the skin-friction coefficient. The effect of distinct values of L_b, P_e, B_n and ω^* along with the microorganism number is presented in Table 4. It was discovered that higher estimates of L_b, P_e and ω^* increase the motile density transfer rate; however, higher values of B_n have the reverse effect. Figure 2 describes the flowchart of bvp4c scheme. The influence of the magnetic parameter (M), volume fraction parameter (ϕ_1), and Stefan blowing parameter (s) on the liquid velocity is indicated in Figures 3–5. It can be noted from Figure 3 that a stronger estimate of M increases the velocity profile. The cause of this pattern is that a magnetic field in an electrically conducting liquid induces a Lorentz force and reduces the momentum boundary layer flow considerably. Figure 4 displays the influence of distinct values of the volume particle parameters versus velocity distribution, and we can perceive that the impact of solid volume fraction enhances thermal transmittance in both solutions, due to the increased number of nanoparticles in the fluid system, which increases resistance while also improving boundary layer thicknesses. Figure 5 displays the effect of the Stefan blowing characteristic on the fluid velocity. It can be noted that the fluid velocity is increased due to a higher estimate of s. Physically, buoyancy forces emerge as a result of the blowing effect, which intensify fluid movement and transport heated nanofluid away from the surface. The influence of the volume fraction parameter (ϕ_1), thermal Biot number (B_e), Eckert number (E_c), and thermal relaxation characteristic (γ_e) on the thermal field is presented in Figures 6–9. It can be seen from Figure 6 that larger values of ϕ_1 increase the fluid temperature because, due to a larger ϕ_1, a retardation effect takes place, which boosts the temperature. The effect of the Biot number on the temperature is described in Figure 7. The Biot number, in reality, includes the heat transfer coefficient. As the Biot number increases, so does the heat transmission coefficient. The fluid temperature and the related boundary layer thickness increase as the heat transport coefficient increases. Figure 8 depicts the features of E_c in the temperature distribution. High Eckert numbers cause the fluid temperature to rise faster because the fluid particles move faster, allowing them to collide more frequently and produce heat, causing the fluid temperature to rise faster. Figure 9 shows that an increase in the value of the thermal relaxation characteristic reduces the temperature. Physically, this is because the time it takes for material particles to transfer heat to adjacent particles reduces when γ_e is increased. In other words, greater values of γ_e cause the material to

behave in a non-conducting manner, resulting in a drop in fluid temperature. Furthermore, it should be highlighted that for $\gamma_e = 0$, heat is quickly transferred throughout the material. The temperature profile is greater for $\gamma_e = 0$, i.e., in the Fourier's law case, than for the Cattaneo–Christov premise. The influence of the Stefan blowing parameter (s), concentration Biot number (B_c), Lewis number (L_e), and relaxation concentration characteristic (γ_c) on the concentration is described in Figures 10–13. Figure 10 shows that a larger estimate of s reduces the concentration. The effect of B_c on the concentration is shown in Figure 11. Fluid particles require a longer time to diffuse across the material medium as B_c is increased. As a result, the concentration distribution is reduced. Figure 12 shows the varying behavior of γ_c along the concentration distribution. It is drawn showing that a larger assessment of γ_c reduces the concentration. Physically, more time is required to transport the nanoparticles from one place to another. The impact of the Lewis number on the concentration is seen in Figure 13. It is interesting to note that L_e is the ratio between thermal and mass diffusivity; as we increase L_e, the mass diffusivity increases, and as a consequence the concentration profile declines. The influence of the bio-convection Lewis parameter (L_b), Peclet number (P_e), and microorganism Biot number (B_n) on the microorganism density is shown in Figures 14–16. It can be seen from Figures 14 and 15 that larger values of L_b and P_e reduce the microorganism density profile. Physically, with an increment in L_b and P_e, the microorganism diffusivity declines, and as a result both curves are reduced. Figure 16 shows the behavior of B_n against the microorganism density profile. It shows that the microorganism density profile is enhanced due toa larger estimation of B_n.

Table 3. The $f''(0)$ (local skin friction coefficient), along with other parameters.

ϕ_1	M	α	s	$Re_x^{1/2} C_f$
0.0	1.0	50°	1.0	0.62880
0.01				0.68261
0.02				0.70860
	2.0			0.65672
	3.0			0.64121
	4.0			0.62612
		0°		0.26505
		30°		0.24703
		45°		0.22704
			0.2	0.34735
			0.3	0.32034
			0.4	0.30347

Table 4. $Re_x^{-1/2}\, Nn_x$, along with other parameters.

L_b	P_e	B_n	ω^*	$Re_x^{1/2}\, Nn_x$
0.5	0.4	0.2	$\pi/4$	3.84684
0.6				3.92359
0.7				3.99025
	0.1			3.49515
	0.3			3.58288
	0.5			3.67057
		0.4		3.83391
		0.5		3.81670
		0.6		3.80203
			$5\pi/12$	3.88790
			$11\pi/24$	3.92790
			$\pi/2$	3.96792

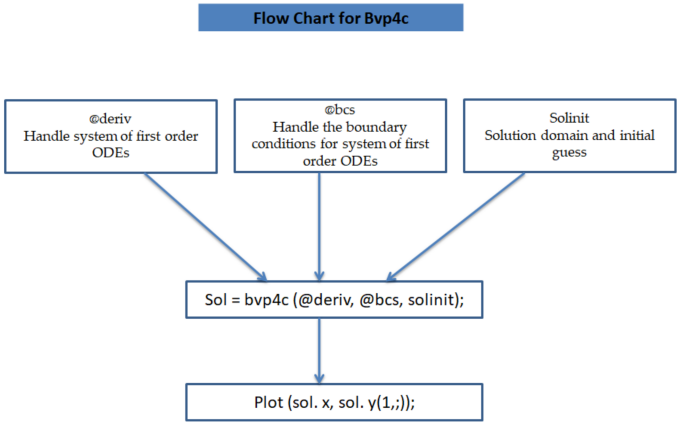

Figure 2. Flowchart of bvp4c scheme.

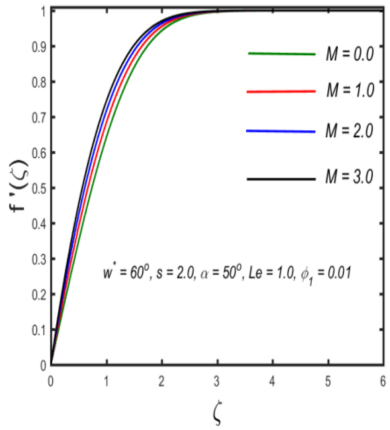

Figure 3. Variation in the velocity against magnetic parameter.

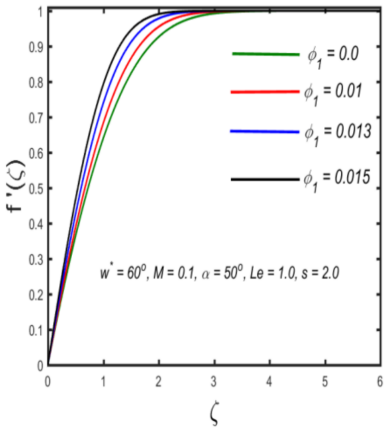

Figure 4. Variation in the velocity profile against solid volume fraction.

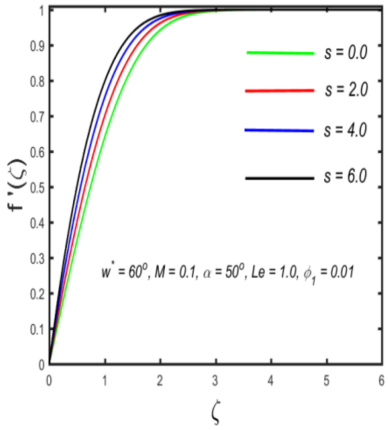

Figure 5. The effect of velocity along with Stefan blowing parameter.

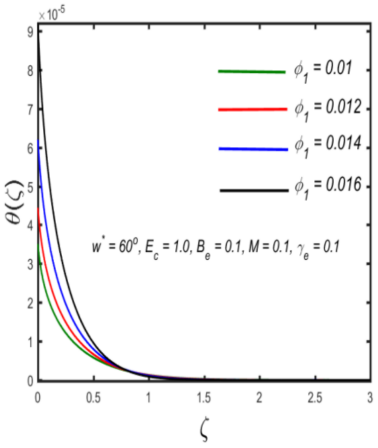

Figure 6. The effect of temperature against solid volume fraction.

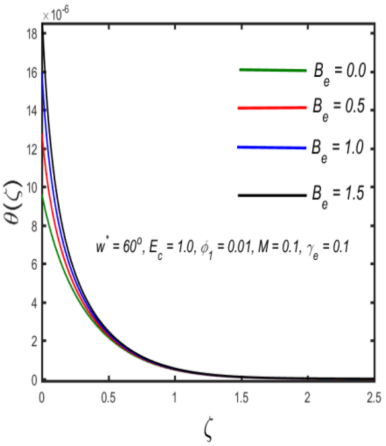

Figure 7. The effect of temperature against thermal Biot number.

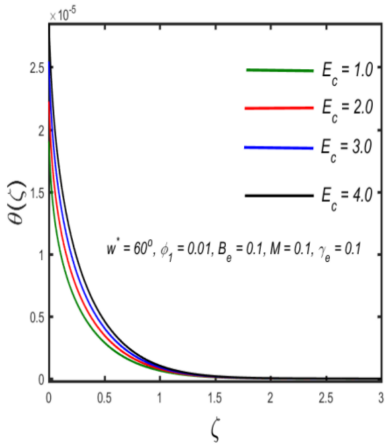

Figure 8. Variation in the temperature against Eckert number.

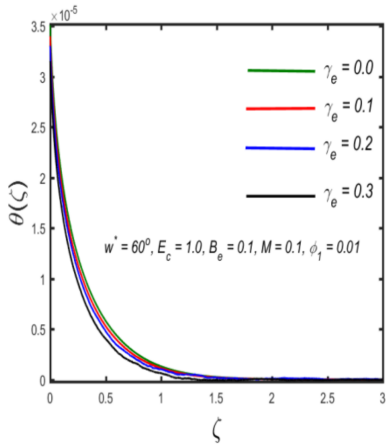

Figure 9. Variation in temperature against thermal relaxation parameter.

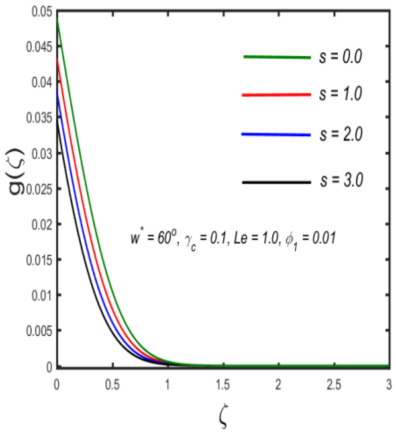

Figure 10. The effect of concentration against Stefan blowing parameter.

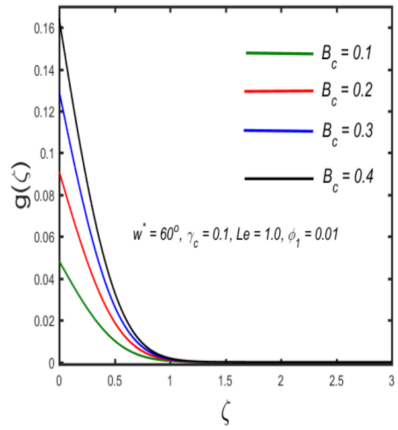

Figure 11. Graph of concentration against concentration Biot number.

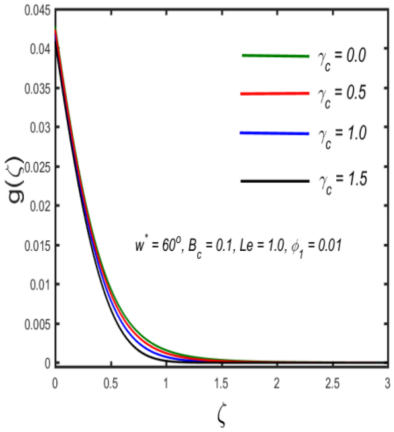

Figure 12. The effect of concentration against concentration relaxation parameter.

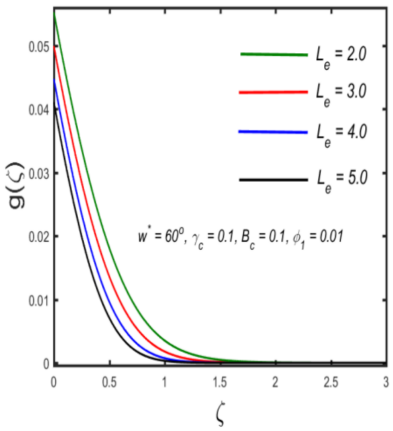

Figure 13. The effect of concentration against Lewis number.

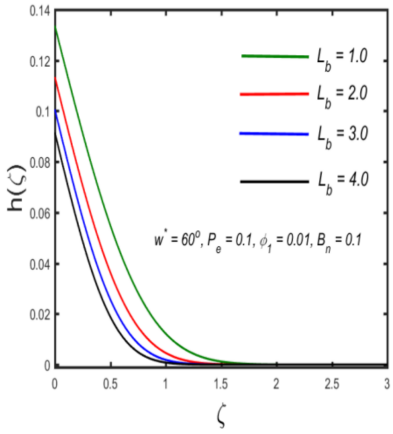

Figure 14. The effect of the density of motile microorganisms against bio-convection Lewis parameter.

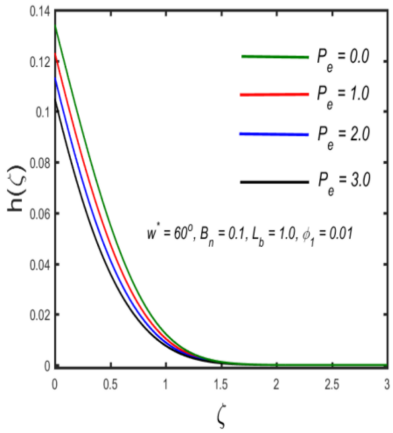

Figure 15. The effect of the density of motile microorganisms against Peclet number.

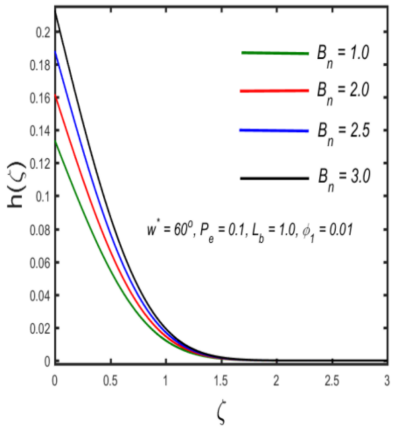

Figure 16. The effect of the density of motile microorganisms against microorganism Biot number.

5. Concluding Remarks

The time-dependent 2D Blasius–Rayleigh–Stokes flow of hybrid nanomaterial liquid with magnetic field and microorganism effects is discussed. Convective conditions are applied at the surface of the extending surface. The main results of the current research are as follows:

1. The velocity of the liquid is increased for higher estimates of the volume fraction parameter and magnetic parameter, due to the retardation effect.

2. Higher values of the Stefan blowing parameter improve the velocity of the liquid and the momentum boundary layer thickness.
3. A decaying trend occurs due to a higher thermal relaxation characteristic because particles have extra time to transport heat to nearby particles.
4. Kinetic energy is transformed into heat energy due to the enhancement of the Eckert number.
5. The nanoparticle concentration declines due to larger estimates of concentration relaxation and Stefan blowing parameter.
6. A higher estimate of thermal and concentration Biot number improves the heat and mass transfer rates, respectively.
7. A decreasing behavior occurs in the microorganism density profile due to larger values of L_b and P_e.
8. The motile density transfer rate decays for larger values of B_n.

Author Contributions: Y.J.: formal analysis, data curation, and writing—review and editing; J.Z.: formal analysis, validation, and writing—review and editing; T.A.: funding acquisition, resources, validation, and writing—review and editing; S.A.: conceptualization, investigation, and writing—original draft; M.N.K.: supervision, visualization, and resources; A.R.: writing—review and editing, validation, and software; A.H.A.: formal analysis, writing—review and editing, and funding acquisition; A.S.E.-S.: investigation, visualization, and writing—review and editing. All authors have read and agreed to the published version of the manuscript.

Funding: The author T. Abdeljawad would like to thank Prince Sultan University for paying the APC and support through the TAS research laboratory. In addition, this project was funded by Taif University Researchers Supporting Project (number TURSP-2020/252), Taif University, Taif, Saudi Arabia.

Data Availability Statement: All data supporting this study are available in the article.

Acknowledgments: The author T. Abdeljawad would like to thank Prince Sultan University for paying the APC and support through the TAS research laboratory. In addition, the authors would like to acknowledge financial support from the Taif University Researchers Supporting Project (number TURSP-2020/252), Taif University, Taif, Saudi Arabia.

Conflicts of Interest: The authors declare no conflict of interest.

Abbreviations

u, v	Velocity components	B_e	Thermal Biot number
x, y	Coordinates	B_c	Concentration Biot number
M	Magnetic parameter	B_n	Microorganism Biot number
B	magnetic field	ω^*	Ablation/accretion parameter
T, T_w	Temperature, and wall temperature	Greek symbols	
D_n	Diffusivity of microorganisms	ρ_{hnf}, ρ_f	Density
Pr	Prandtl number	μ_{hnf}, μ_f	Dynamic viscosity
C_p	Specific heat	τ_{xy}	Shear stress
U_w	Stretching velocity along the x-direction	α_{hnf}, α_f	Modified thermal diffusivity
D_m	Brownian diffusion coefficient	$(\rho C_p)_{hnf'}$ $(\rho C_p)_f$	Heat capacity
E_c	Eckert number	k_f, k_{hnf}	Thermal conductivity

C_f	Surface drag force	ϕ_1	The solid volume fraction of particles
Nu_x	Nusselt number	ζ	Scaled boundary-layer coordinate
P_e	Bioconvection Péclet number	σ_{hnf}, σ_f	Electric conductivity
b	Chemotaxis constants	λ_1	Thermal relaxation time
s	Stefan blowing parameter	λ_1	Concentration relaxation time
L_e	Lewis number	γ_e	Thermal relaxation parameter
W_c	Maximum cell swimming speed	γ_c	Concentration relaxation characteristic
L_b	Bio-convection Lewis number	θ	Dimensionless temperature
h_h, h_g, h_n	Heat, mass, and microorganism transport coefficients, respectively		
Subscripts			
w	The boundary surface	∞	The ambient surface
hnf	Hybrid nanofluid	nf	Nanofluid

References

1. Choi, S.U.; Eastman, J.A. *Enhancing Thermal Conductivity of Fluids with Nanoparticles*; No. ANL/MSD/CP-84938; CONF-951135-29; Argonne National Lab.: DuPage County, IL, USA, 1995.
2. Buongiorno, J. Convective Transport in Nanofluids. *J. Heat Transfer.* **2006**, *128*, 240–250. [CrossRef]
3. Sheikholeslami, M.; Chamkha, A.J. Influence of Lorentz forces on nanofluid forced convection considering Marangoni convection. *J. Mol. Liq.* **2017**, *225*, 750–757. [CrossRef]
4. Ahmad, S.; Nadeem, S.; Muhammad, N.; Issakhov, A. Radiative SWCNT and MWCNT nanofluid flow of Falkner–Skan problem with double stratification. *Phys. A Stat. Mech. Its Appl.* **2020**, *547*, 124054. [CrossRef]
5. Hymavathi, T.; Mathews, J.; Kiran Kumar, R.V.M.S.S. Heat transfer and inclined magnetic field effects on un-steady free convection flow of MoS2 and MgO–water based nanofluids over a porous stretching sheet. *Int. J. Ambient. Energy* **2021**, 1–9. [CrossRef]
6. Nadeem, S.; Ahmad, S.; Muhammad, N. Analysis of ferrite nanoparticles in liquid. *Pramana* **2020**, *94*, 54. [CrossRef]
7. Muhammad, N.; Nadeem, S. Ferrite nanoparticles Ni-$ZnFe_2O_4$, Mn-$ZnFe_2O_4$ and Fe_2O_4 in the flow of ferro-magnetic nanofluid. *Eur. Phys. J. Plus* **2017**, *132*, 377. [CrossRef]
8. Vajravelu, K.; Prasad, K.V.; Lee, J.; Lee, C.; Pop, I.; Van Gorder, R.A. Convective heat transfer in the flow of vis-cous Ag–water and Cu–water nanofluids over a stretching surface. *Int. J. Therm. Sci.* **2011**, *50*, 843–851. [CrossRef]
9. Jamshed, W.; Devi, S.U.S.; Goodarzi, M.; Prakash, M.; Nisar, K.S.; Zakarya, M.; Abdel-Aty, A.-H. Evaluating the unsteady Casson nanofluid over a stretching sheet with solar thermal radiation: An optimal case study. *Case Stud. Therm. Eng.* **2021**, *26*, 101160. [CrossRef]
10. Sheikholeslami, M. Influence of Lorentz forces on nanofluid flow in a porous cylinder considering Darcy mod-el. *J. Mol. Liq.* **2017**, *225*, 903–912. [CrossRef]
11. Ahmad, S.; Nadeem, S. Flow analysis by Cattaneo–Christov heat flux in the presence of Thomson and Troian slip condition. *Appl. Nanosci.* **2020**, *10*, 4673–4687. [CrossRef]
12. Rostami, S.; Afrand, M.; Shahsavar, A.; Sheikholeslami, M.; Kalbasi, R.; Aghakhani, S.; Shadloo, M.S.; Oztop, H.F. A review of melting and freezing processes of PCM/nano-PCM and their application in energy storage. *Energy* **2020**, *211*, 118698. [CrossRef]
13. Mingzheng, Z.; Guodong, X.; Jian, L.; Lei, C.; Lijun, Z. Analysis of factors influencing thermal conductivity and viscosity in different kinds of surfactant solutions. *Exp. Therm. Fluid Sci.* **2012**, *36*, 22–29. [CrossRef]
14. Ahmad, S.; Nadeem, S.; Ullah, N. Entropy generation and temperature-dependent viscosity in the study of SWCNT–MWCNT hybrid nanofluid. *Appl. Nanosci.* **2020**, *10*, 5107–5119. [CrossRef]
15. Anuar, N.S.; Bachok, N.; Pop, I. Influence of buoyancy force on Ag-MgO/water hybrid nanofluid flow in an in-clined permeable stretching/shrinking sheet. *Int. Commun. Heat Mass Transf.* **2021**, *123*, 105236. [CrossRef]
16. Maskeen, M.M.; Zeeshan, A.; Mehmood, O.U.; Hassan, M. Heat transfer enhancement in hydromagnetic alumina–copper/water hybrid nanofluid flow over a stretching cylinder. *J. Therm. Anal.* **2019**, *138*, 1127–1136. [CrossRef]
17. Ghalambaz, M.; Sheremet, M.A.; Mehryan, S.A.M.; Kashkooli, F.M.; Pop, I. Local thermal non-equilibrium anal-ysis of conjugate free convection within a porous enclosure occupied with Ag–MgO hybrid nanofluid. *J. Therm. Anal. Calorim.* **2019**, *135*, 1381–1398. [CrossRef]

18. Manna, N.K.; Mondal, C.; Biswas, N.; Sarkar, U.K.; Öztop, H.F.; Abu-Hamdeh, N.H. Effect of multibanded mag-netic field on convective heat transport in linearly heated porous systems filled with hybrid nanofluid. *Phys. Fluids* **2021**, *33*, 053604. [CrossRef]
19. Ahmad, S.; Nadeem, S. Analysis of activation energy and its impact on hybrid nanofluid in the presence of Hall and ion slip currents. *Appl. Nanosci.* **2020**, *10*, 5315–5330. [CrossRef]
20. Esfe, M.H.; Arani, A.A.A.; Rezaie, M.; Yan, W.M.; Karimipour, A. Experimental determination of thermal con-ductivity and dynamic viscosity of Ag–MgO/water hybrid nanofluid. *Int. Commun. Heat Mass Transf.* **2015**, *66*, 189–195. [CrossRef]
21. Rana, P.; Makkar, V.; Gupta, G. *Finite Element Modelling of MHD Stefan Blowing Convective Ag-MgO/Water Hybrid Nanofluid induced by Stretching Cylinder utilizing Non-Fourier/Ficks Model*; Research Square: Durham, NC, USA, 2021.
22. Ma, Y.; Mohebbi, R.; Rashidi, M.M.; Yang, Z. MHD convective heat transfer of Ag-MgO/water hybrid nanofluid in a channel with active heaters and coolers. *Int. J. Heat Mass Transf.* **2019**, *137*, 714–726. [CrossRef]
23. Fourier, J.B.J. *Théorie Analytique De La Chaleur*; Académie des Sciences: Paris, France, 1822; p. 3.
24. Fick, A. Poggendorff's flannel. *Physik* **1855**, *94*, 297.
25. Cattaneo, C. Sulla Conduzione Del Calore. In *Some Aspects of Diffusion Theory*; Springer: Berlin/Heidelberg, Germany, 2011; Volume 3, p. 485. [CrossRef]
26. Christov, C. On frame indifferent formulation of the Maxwell–Cattaneo model of finite-speed heat conduction. *Mech. Res. Commun.* **2009**, *36*, 481–486. [CrossRef]
27. Han, S.; Zheng, L.; Li, C.; Zhang, X. Coupled flow and heat transfer in viscoelastic fluid with Cattaneo–Christov heat flux model. *Appl. Math. Lett.* **2014**, *38*, 87–93. [CrossRef]
28. Venkateswarlu, S.; Varma, S.V.K.; Durga Prasad, P. MHD Flow of MoS2 and MgO water-based nanofluid through porous medium over a stretching surface with Cattaneo-Christov heat flux model and convective boundary condition. *Int. J. Ambient. Energy* **2020**, 1–10. [CrossRef]
29. Ali, B.; Hussain, S.; Abdal, S.; Mehdi, M.M. Impact of Stefan blowing on thermal radiation and Cattaneo–Christov characteristics for nanofluid flow containing microorganisms with ablation/accretion of leading edge: FEM approach. *Eur. Phys. J. Plus* **2020**, *135*, 821. [CrossRef]
30. Ahmad, S.; Nadeem, S.; Muhammad, N.; Khan, M.N. Cattaneo–Christov heat flux model for stagnation point flow of micropolar nanofluid toward a nonlinear stretching surface with slip effects. *J. Therm. Anal.* **2021**, *143*, 1187–1199. [CrossRef]
31. Raju, C.S.K.; Sanjeevi, P.; Raju, M.C.; Ibrahim, S.M.; Lorenzini, G.; Lorenzini, E. The flow of magnetohydrody-namic Maxwell nanofluid over a cylinder with Cattaneo–Christov heat flux model. *Contin. Mech. Thermodyn.* **2017**, *29*, 1347–1363. [CrossRef]
32. Malik, R.; Khan, M.; Mushtaq, M. Cattaneo-Christov heat flux model for Sisko fluid flow past a permeable non-linearly stretching cylinder. *J. Mol. Liq.* **2016**, *222*, 430–434. [CrossRef]
33. Jamshed, W.; Aziz, A. Cattaneo–Christov based study of TiO_2–CuO/EG Casson hybrid nanofluid flow over a stretching surface with entropy generation. *Appl. Nanosci.* **2018**, *8*, 685–698. [CrossRef]
34. Garia, R.; Rawat, S.K.; Kumar, M.; Yaseen, M. Hybrid nanofluid flow over two different geometries with Catta-neo–Christov heat flux model and heat generation: A model with correlation coefficient and probable error. *Chin. J. Phys.* **2021**, *74*, 421–439. [CrossRef]
35. Sahoo, B. Effects of slip, viscous dissipation and Joule heating on the MHD flow and heat transfer of a second grade fluid past a radially stretching sheet. *Appl. Math. Mech.* **2010**, *31*, 159–173. [CrossRef]
36. Shehzad, S.A.; Alsaedi, A.; Hayat, T. Influence of thermophoresis and joule heating on the radiative flow of jeffrey fluid with mixed convection. *Braz. J. Chem. Eng.* **2013**, *30*, 897–908. [CrossRef]
37. Waqas, H.; Farooq, U.; Khan, S.A.; Alshehri, H.M.; Goodarzi, M. Numerical analysis of dual variable of conduc-tivity in bioconvection flow of Carreau–Yasuda nanofluid containing gyrotactic motile microorganisms over a porous me-dium. *J. Therm. Anal. Calorim.* **2021**, *145*, 2033–2044. [CrossRef]
38. Kumar, K.G.; Ramesh, G.K.; Gireesha, B.; Gorla, R. Characteristics of Joule heating and viscous dissipation on three-dimensional flow of Oldroyd B nanofluid with thermal radiation. *Alex. Eng. J.* **2018**, *57*, 2139–2149. [CrossRef]
39. Hayat, T.; Khan, M.I.; Alsaedi, A. Joule heating and viscous dissipation in flow of nanomaterial by a rotating disk. *Int. Commun. Heat Mass Transf.* **2017**, *89*, 190–197. [CrossRef]
40. Chakraborty, R.; Dey, R.; Chakraborty, S. Thermal characteristics of electromagnetohydrodynamic flows in nar-row channels with viscous dissipation and Joule heating under constant wall heat flux. *Int. J. Heat Mass Transf.* **2013**, *67*, 1151–1162. [CrossRef]
41. Chen, C.H. Combined effects of Joule heating and viscous dissipation on magnetohydrodynamic flow past a per-meable, stretching surface with free convection and radiative heat transfer. *J. Heat Transf.* **2010**, *132*, 064503. [CrossRef]
42. Na, T. Boundary layer flow of Reiner-Philippoff fluids. *Int. J. Non-Linear Mech.* **1994**, *29*, 871–877. [CrossRef]
43. Fang, T. A note on the unsteady boundary layers over a flat plate. *Int. J. Non-Linear Mech.* **2008**, *43*, 1007–1011. [CrossRef]
44. Todd, L. A family of laminar boundary layers along a semi-infinite flat plate. *Fluid Dyn. Res.* **1997**, *19*, 235–249. [CrossRef]
45. Reddy, M.G.; Rani, M.S.; Kumar, K.G.; Prasannakumar, B.C.; Chamkha, A.J. Cattaneo–Christov heat flux model on Blasius–Rayleigh–Stokes flow through a transitive magnetic field and Joule heating. *Phys. A Stat. Mech. Its Appl.* **2020**, *548*, 123991. [CrossRef]
46. Ahmad, A. Flow of ReinerPhilippoff based nano-fluid past a stretching sheet. *J. Mol. Liq.* **2016**, *219*, 643–646. [CrossRef]
47. Mabood, F.; Khan, W.A. A computational study of unsteady radiative magnetohydrodynamic Blasius and Sakiadis flow with leading-edge accretion (ablation). *Heat Transf.* **2020**, *49*, 1355–1373. [CrossRef]

48. Sajid, T.; Jamshed, W.; Shahzad, F.; Eid, M.R.; Alshehri, H.M.; Goodarzi, M.; Akgül, E.K.; Nisar, K.S. Micropolar fluid past a convectively heated surface embedded with nth order chemical reaction and heat source/sink. *Phys. Scr.* **2021**, *96*, 104010. [CrossRef]
49. Ahmad, S.; Naveed Khan, M.; Rehman, A.; Felemban, B.F.; Alqurashi, M.S.; Alharbi, F.M.; Galal, A.M. Analysis of Heat and Mass Transfer Features of Hybrid Casson Nanofluid Flow with the Magnetic Dipole Past a Stretched Cylin-der. *Appl. Sci.* **2021**, *11*, 11203. [CrossRef]